Alexandria Engineering Journal 108 (2024) 206–220

Contents lists available at ScienceDirect

Alexandria Engineering Journal

journal homepage: www.elsevier.com/locate/aej

Green auto-combustion synthesis of $SrNiO_3/NiO/SrCO_3$ ferromagnetic-nanocomposites in the presence carbohydrate sugars and their application as photocatalyst for degradation of water-soluble organic-pollutants

Seyed Amirhossein Ehsanizadeh [a], Mojgan Goudarzi [b], Elmuez A. Dawi [c], Forat H. Alsultany [d], Aseel M. Aljeboree [e], Masoud Salavati-Niasari [a,*]

[a] Institute of Nano Science and Nano Technology, University of Kashan, P.O. Box. 87317-51167, Kashan, IR, Iran
[b] Institute of Nanotechnology, Karlsruhe Instituteof Technology, Hermann-von-Helmholtz-Platz 1, Eggenstein-Leopoldshafen 76344, Germany
[c] College of Humanities and Sciences, Department of Mathematics, and Science, Ajman University, P.O. Box 346, Ajman, the United Arab Emirates
[d] Department of Medical Physics, College of Sciences, Al-Mustaqbal University, Babylon 51001, Iraq
[e] Department of Chemistry, College of Science for Women, University of Bbabylon, Hilla, Iraq

ARTICLE INFO

Keywords:
$SrNiO_3/NiO/SrCO_3$ Nanocomposites
Nanostructures
Nano-Photocatalyst
Sun-like light
Scavenger

ABSTRACT

This study utilized an environmentally-friendly method to synthesize $SrNiO_3/NiO/SrCO_3$ nanocomposites using glucose and lactose as fuels. A variety of fuel concentrations were investigated in order to determine their effects on $SrNiO_3/NiO/SrCO_3$ nanocomposites from both a pure and a morphological perspective. Various physiochemical techniques were employed to examine the crystal structure, morphology, optical, magnetic, and surface properties of the synthesized nanoparticles. These techniques included X-ray diffract, scanning electron microscopy, transmission electron microscopy, energy-dispersive spectroscopy (EDS), Fourier-Transform Infrared Spectroscopy (FTIR), vibrating sample magnetometers, and Brunauer-Emmett-Tellers. The band gap of the as-synthesized nanoparticles was determined to be 2.5 eV, suggesting that they are capable of acting as a photocatalyst under sunlight-like conditions. The photocatalytic activity of $SrNiO_3/NiO/SrCO_3$ nanocomposites was evaluated against Methyl orange (MO) and Methyl violet (MV), and the mechanism of the photocatalyst was investigated using EDTA, benzoic acid, and benzoquinone as scavengers. A comparison of photocatalytic activity in UV and sun-like light showed that maximum degradation (92 %) and (84.8 %) were related to degradation of MO (20 ppm) and MV in 60 min, respectively. The results indicate that $SrNiO_3/NiO/SrCO_3$ nanocomposites synthesized using the auto combustion method may serve as a promising photocatalyst for the degradation of organic pollutants in the environment within a short period of time.

1. Introduction

As materials science and environmental conservation continue to evolve, the search for innovative solutions to tackle pollution and wastewater treatment challenges remains paramount. Many studies have been conducted on the use of earth abundant metal oxides as photocatalysts and for the treatment of water waste. Earth-abundant metal oxides are potential photocatalysts due to their high activity and inexpensive cost [1–4]. Most metal oxides, however, have band gaps that are too wide to effectively absorb sun-like light [5–7]. The ABO_3 perovskites are a class of mixed oxides with the general formula ABO3, where A is an ion of lanthanide and/or alkaline earth metal and B is an ion of a transition metal [8]. The A and B sites in ABO_3 can also accommodate cations with a range of charges, leading to a variety of AB combinations with entirely distinct characteristics. Combinations with varied degrees of stability can be created, such as $A^{2+}B^{4+}O_3$ $A^{3+}B^{3+}O_3$, $A^{4+}B^{2+}O_3$, $A^{5+}B^{+}O_3$ and $A^{+}B^{5+}O_3$ [9]. The A or B sites of ABO_3 perovskites may often accommodate most metals from the periodic table, giving rise to materials with tunable photocatalytic characteristics. Perovskite materials are widely used in composites, specifically in solar cells, light-emitting diodes, photodetectors, lasers, and photocatalyst [9–12]. A number of key factors play a significant role in the

* Corresponding author.
E-mail address: Salavati@Kashanu.ac.ir (M. Salavati-Niasari).

https://doi.org/10.1016/j.aej.2024.07.088
Received 15 February 2024; Received in revised form 6 June 2024; Accepted 22 July 2024
Available online 29 July 2024

performance of photocatalysts in photocatalysis. As part of these factors, crystallinity, particle size, shape, defect presence or absence, and specific surface area are considered. Efficacy of photocatalytic processes is determined by the interplay of these characteristics [13–17]. Furthermore, it has been observed that even when employing identical synthesis methods, the morphology of nanoparticles can yield distinct photocatalytic activities [18–21]. This underscores the importance of fine-tuning the structural aspects of photocatalytic materials. When embarking on the synthesis of perovskite materials for photocatalysis, the choice of the synthesis method is a critical step [22–24]. In making this decision, a number of factors must be considered, including economic factors, the simplicity of the method, the availability of precursors, as well as the quality and yield of the resulting products. The various synthesis methods can produce materials with varying morphologies, crystal structures, optical properties, and surface areas, as well as photocatalytic properties [25–27]. One promising avenue in enhancing photocatalytic properties involves coupling ABO_3 materials with other semiconductor nanoparticles. This approach has been extensively explored and has shown promise in boosting catalytic activity. The enhancement stems from an amalgamation of factors, including improved photo response, heightened charge separation efficiency, and the presence of multiple active sites within hybrid nanostructures [28,29]. These perovskite nanocomposites can range from straightforward binary nanostructures to more intricate ternary and quaternary combinations [30,31]. This diversity allows for tailoring materials with unique and improved photocatalytic properties, ushering in a new era of advanced photocatalysis. Investigating perovskite materials with $ANiO_3$ (A = Sr, Mn, Ce, La and Ca) is one of the project's most promising directions. These perovskites, albeit less explored than their more well-known siblings, have intriguing features that make them useful for thermoelectric devices, methane reforming, photocatalysis, electrical components, and water splitting [32]. This article embarks on a comprehensive journey through the realm of perovskite materials, focusing on the synthesis, properties, and diverse applications of $SrNiO_3/NiO/SrCO_3$ nanocomposites. We will also highlight their remarkable potential in the photodegradation of persistent organic pollutants. Before delving into the specifics of $SrNiO_3/NiO/SrCO_3$ nanocomposites, it is essential to comprehend the pressing need for advanced photocatalytic materials. Substances like methyl orange and methyl violet, commonly used as dyes in various industries, pose significant environmental hazards due to their persistence in water bodies. Traditional wastewater treatment methods often fall short in completely removing these pollutants, resulting in contaminated water sources and ecological harm [33]. This is where the exceptional capabilities of $SrNiO_3/NiO/SrCO_3$ nanocomposites come into play. The journey into the world of perovskite materials begins with an exploration of their foundational characteristics. Perovskites, a unique class of compounds characterized by their distinctive crystal structure, exhibit exceptional properties that make them intriguing for various applications. Among these, $SrNiO_3$, a notable perovskite compound, stands out as a primary building block in the creation of the innovative $SrNiO_3/NiO/SrCO_3$ nanocomposites. Examining the broader landscape of NiO_3-based perovskites, we discover a spectrum of applications that have captured the attention of researchers and scientists. NiO_3-based perovskites have shown remarkable promise in water splitting a critical process for harnessing renewable energy through hydrogen production [34]. These materials facilitate the separation of water into its constituent elements, hydrogen and oxygen, using solar energy. This application holds immense potential for clean and sustainable energy generation, offering a pathway to a greener future. Beyond energy, NiO_3-based perovskites have found utility in the world of electronic components. Their unique electronic properties open up avenues for the development of advanced devices and technologies [35]. These materials contribute to the creation of high-performance sensors, transistors, and other electronic components, propelling the electronics industry forward. Another exciting domain of application lies in thermoelectric devices, where NiO_3-based perovskites play a pivotal role in converting heat into electrical energy [36]. This innovation holds the potential for waste heat recovery and the advancement of energy-efficient technologies, thus contributing to sustainability. In the pursuit of sustainable energy production, NiO_3-based perovskites are being actively investigated for methane reforming [37]. This process transforms methane, a potent greenhouse gas, into hydrogen and solid carbon, offering a promising solution to mitigate methane emissions and combat climate change. The photocatalytic properties of these perovskites extend beyond wastewater treatment. They are also employed in the degradation of organic pollutants and the removal of harmful contaminants from the environment. The efficiency of these materials under sun-like light makes them highly attractive for eco-friendly photocatalysis, addressing pollution and water treatment challenges [38]. While these applications showcase the versatility of NiO_3-based perovskites, it is important to recognize that there is still untapped potential within this class of materials. Further research and exploration are needed to fully harness their capabilities and unlock new possibilities in materials science and environmental conservation. Notably, $SrNiO_3/NiO/SrCO_3$ nanocomposites distinguish themselves by their exceptional efficiency in a short time frame a crucial advantage in environmental remediation. Many advanced oxide catalysts and photocatalysts exhibit commendable performance over extended periods, typically in the range of 360–450 minutes. However, $SrNiO_3/NiO/SrCO_3$ nanocomposites have demonstrated their prowess with impressive results, achieving a best performance of 92 % for the degradation of methyl orange and 84.8 % for methyl violet in just 60 minutes. This remarkable speed in pollutant removal sets them apart in the realm of photocatalysis under sun-like light. In the following sections, we will delve into the specific attributes of $SrNiO_3/NiO/SrCO_3$ nanocomposites, unveiling their synthesis methods and shedding light on their remarkable efficiency in the photodegradation of persistent organic pollutants under sun-like light. Additionally, we will explore the limited existing reports on these nanocomposites, aiming to provide a comprehensive understanding of their potential in addressing the pressing challenges of pollution and wastewater treatment. Our exploration into the world of perovskite materials and their applications promises to illuminate a path towards a cleaner and more sustainable future.

2. Materials and methods

2.1. Materials

All of the chemical materials that used in this study were pure and used without any purifications. The chemical substrate including Sr $(NO_3)_2$ (M_W = 211.63 g.mol^{-1}, purity percent ≥ 99.9 %) Ni $(NO_3)_2.6\,H_2O$ (M_W = 290.81 g.mol^{-1}, purity percent ≥ 99.9 %) Lactose ($C_{12}H_{22}O_{11}$)(M_W = 342.3 g.mol^{-1}), Glucose monohydrate ($C_6H_{12}O_6.H_2O$) (M_W = 198.17 g.mol^{-1}), EDTA (M_W = 372.24 g.mol^{-1}, purity percent ≥ 99.9 %), Benzoic acid (M_W = 122.12 g.mol^{-1}, purity percent ≥ 99.9 %) and Benzoquinone acid (M_W = 108.095 g.mol^{-1}, purity percent ≥ 99.9 %).

2.2. Synthesis method of $SrNiO_3/NiO/SrCO_3$ nanocomposites

In this study, $SrNiO_3/NiO/SrCO_3$ nanostructures were synthesized using the auto-combustion method (Fig. 1). Glucose and lactose served as the fuel for the reaction. Initially, 0.2000 g (0.9 mmol) of Sr $(NO_3)_2$ and 0.2748 g of Ni $(NO_3)_2{\cdot}6\,H_2O$ (0.9 mmol) were separately dissolved in 20 ml of distilled water to form two clear solutions. Subsequently, glucose or lactose with varying stoichiometric ratios by weight were dissolved in 20 ml of distilled water. Both glucose and lactose played dual roles as fuel and capping agents to prevent the formation of agglomerated particles. The Sr solution was placed on a heated stirrer, and the solution's temperature was gradually raised to 60 °C. The fuel solution was added dropwise to the Sr solution under magnetic stirring.

Fig. 1. : Schematic of the synthesis of $SrNiO_3/NiO/SrCO_3$ nanocomposites.

After 15 minutes, the green Ni solution was introduced into the mixture. The temperature of the mixed solution was slowly increased to 120 °C and maintained at this temperature under magnetic stirring for 120 minutes. At this temperature, combustion occurred, resulting in the formation of a sponge-like milky gel. The obtained gel was dried in an oven at 60 °C for 24 hours. The dried gel was calcinated in an electric furnace for 5 hours at different temperatures, including 700, 800, and 900 °C for different samples. The black powder obtained from the calcination process was washed three times with distilled water, ethanol, and methanol to obtain the pure product. Finally, the powder was dried in an oven at 60 °C for 24 h. In addition to the synthesis of $SrNiO_3/NiO/SrCO_3$ nanocomposites using the auto-combustion method with glucose and lactose as fuel sources, a blank sample was prepared using a co-precipitation method. This blank sample served as a control group, representing the absence of added fuel sources in the synthesis process. Initially, solutions of Sr $(NO_3)_2$ and Ni $(NO_3)_2{\cdot}6\ H_2O$ were separately dissolved in distilled water. These solutions were then combined, resulting in the co-precipitation of the desired materials. The obtained precipitate underwent subsequent drying, calcination, and washing steps, following the same procedures outlined for the other samples.

The synthesis of the blank sample provides a baseline for comparison, allowing for a comprehensive evaluation of the effects of different fuel sources on the final product's properties and performance. Details of the synthesis conditions for different samples can be found in Table 1.

2.3. Photocatalyst set up

To assess the photocatalytic activity of $SrNiO_3/NiO/SrCO_3$ nanostructures, a rigorous experimentation process was devised, utilizing two common organic pollutants, Methyl Orange and Methyl Violet, as representative compounds. These pollutants were chosen due to their prevalence in environmental contamination scenarios [39,40]. The study delved into an intricate examination of various parameters affecting the photocatalytic performance. This encompassed a systematic exploration of the impact of dye concentration, catalyst dosage, pH level, and the light source [41–43]. Dye concentrations were meticulously tested at 20, 25, and 30 parts per million (ppm), covering a range of typical pollutant concentrations found in real-world scenarios. In parallel, different nano-catalyst dosages of 0.01, 0.03, and 0.05 g were investigated to optimize the catalytic efficiency. The pH of the dye solution, which can significantly influence the photocatalytic process, was thoughtfully adjusted to 3, 7, and 11, reflecting a spectrum of environmental pH conditions. Furthermore, to simulate diverse lighting conditions encountered in the field, two distinct light sources were employed. The first was the intense and germicidal UV light, known for its efficiency in photocatalysis, and the second was a simulated sunlight source designed to mimic natural light conditions. The photocatalytic tests were meticulously conducted in a controlled environment. A solution of each dye was separately prepared, and $SrNiO_3/NiO/SrCO_3$ nanostructures were carefully dispersed in 50 ml of the respective dye solution. The mixture underwent a 30-minute stirring period in complete darkness to ensure the thorough adsorption of the dyes onto the photocatalyst's surface. Subsequently, the experimental setup involved the activation of a Xenon arc lamp, a versatile light source chosen for its suitability in simulating various lighting conditions. Over the course of the experiment, at 10-minute intervals, 5 ml of the solution was carefully withdrawn and placed in a dark environment, allowing for further reaction in the absence of light for 24 hours. Following this period, the

Table 1
Reaction conditions for synthesis of $SrNiO_3/NiO$ nanostructures and summarized XRD and SEM data.

Sample No.	Fuel	Fuel: Metal (Sr)	Calcination temperature (^{0}C)	XRD/Grain size (nm)	SEM/range size (nm)	Shape
1	Glucose	2:1	700	32.43	-	-
2	Glucose	2:1	800	35.66	-	-
3	Glucose	2:1	900	31.47	80.34	Agglomerated particles
4	Lactose	1:1	900	38.05	65.05	Agglomerated particles
5	Lactose	2:1	900	30.83	85	Uniform particles
6	Lactose	4:1	900	36.84	109.90	Bulk structures
7	blank	-	900	33.07	80.53	Large particles

withdrawn solutions were subjected to centrifugation to separate any remaining particles. The light absorbance of the resulting clear solutions was meticulously measured using an advanced ultraviolet spectrophotometer, specifically, the UV-Visible Spectrophotometer model V-730 from Jasco. The degradation of each dye through photocatalysis was treated as a pseudo-first-order reaction, and its kinetics were mathematically described using a specific formula. This rigorous analytical approach allowed for a comprehensive understanding of the photocatalytic activity's efficiency and provided invaluable insights into the degradation kinetics of these organic pollutants.

3. Result and discussion

3.1. Investigating the structural evolution

In our quest to comprehend the intricate changes within the samples, we conducted X-ray Diffraction (XRD) analysis after calcining the specimens using different fuels and at various calcination temperatures. The primary aim was to determine the presence or absence of the desired compound and to identify the phases existing within the samples. Following calcination at 700°C for 5 hours using glucose as the fuel, XRD analysis of a sample 1 with a 1:2 ratio of strontium metal to glucose yielded an unexpected revelation in Fig. 2(a). The analysis indicated that the intended compound, $SrNiO_3$, had not formed. Instead, the patterns revealed a combination of nanoscale NiO and $SrCO_3$ particles, signifying an incomplete chemical transformation. To delve deeper into the nuances of our samples, we escalated the calcination temperature to 800°C and then 900°C related to sample 2 and 3 that shown in Fig. 2(b) and (c) respectively. This escalation led to a significant shift in the XRD patterns. At these higher temperatures, the presence of $SrNiO_3$ became apparent. However, the phases of NiO and $SrCO_3$ persisted alongside it, highlighting the complexity of coexisting compounds under these conditions. In an effort to eliminate these unwanted phases, a critical alteration made by substituting glucose with lactose as the fuel source. Samples were synthesized at ratios of 1:1, 2:1, and 4:1 of lactose to strontium (sample 4, sample 5 and sample 6), dried, and subjected to calcination at 900°C for 5 hours. As shown in Fig. 3(a), (b) and (c) that related to XRD patterns of sample 4, sample 5 and sample 6 respectively, notably, samples prepared with lactose exhibited substantially reduced $SrCO_3$ content, suggesting a successful reduction of this phase. Furthermore, a blank sample (sample 7), devoid of any fuel source, was included in our

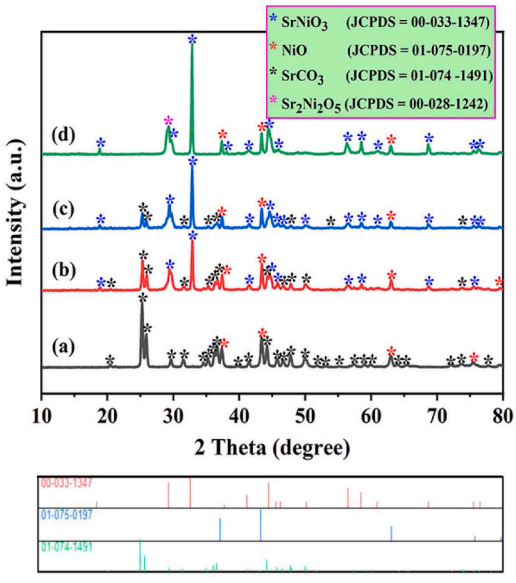

Fig. 2. : XRD patterns of $SrNiO_3$/NiO nanostructures sample 1 (a), sample 2 (b), sample 3 (c) and sample 7 (d).

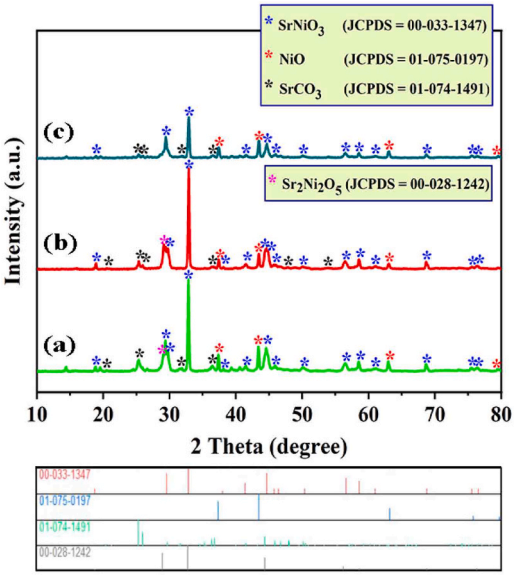

Fig. 3. : XRD patterns of $SrNiO_3$/NiO nanostructures sample 4 (a), sample 5 (b) and sample 6 (c).

analysis. XRD results from this blank sample confirmed the absence of $SrCO_3$ that is obvious in Fig. 2(d). Remarkably, NiO remained consistently present across all conditions, demonstrating its resistance to elimination throughout our experiments. The crystal size of the samples calculated by Debye-Scherrer formula and summarized in Table 1 [44].

3.2. Morphology and chemical purity analysis

To investigate the influence of reaction conditions on the morphology and size of $SrNiO_3$/NiO/$SrCO_3$ nanostructures, SEM analysis was performed. In Fig. 4(a) and (b), the SEM images of Sample 3, portraying $SrNiO_3$/NiO nanostructures, reveal particle agglomeration, resulting in irregular rock-shaped structures. This observation underscores the necessity of adjusting the reaction conditions to achieve improved morphology and size. The size distribution, as depicted in Fig. 4(c) and analyzed using Digimizer, indicates a mean particle size of 80.34 nm [45]. However, due to the agglomeration and absence of ultra-fine particle shapes and sizes, these outcomes were less than satisfactory. The initial optimization parameter focused on the choice of fuel. The condition transitioned to using lactose for Sample 4, and the SEM images and particle size distribution are presented in Fig. 4(d), (e), and (f). These images reveal improved separation in particle morphology, affirming that lactose functions as a more effective capping agent in this reaction.

Nonetheless, it became evident that the capping agent alone was insufficient to achieve the desired particle formation. To address this, the fuel-to-Sr ratio increased to 2:1 and prepared Sample 5. The SEM images in Fig. 5(a) and (b) illustrate that $SrNiO_3$/NiO/$SrCO_3$ particles now maintain a consistent round shape and exhibit better separation, resulting in a narrower size distribution around 85 nm (Fig. 5(c)). Subsequently, we further elevated the fuel-to-Sr ratio to 4:1 for Sample 6. The SEM images in Fig. 5(d) and (e) demonstrate that the higher lactose content, acting as both a fuel and capping agent, introduced diversifying effects on morphology. However, this increase also led to larger particle sizes and increased agglomeration. The particle size distribution in Fig. 5(f) reveals a mean size of 109.9 nm, which did not align with the objectives of our study. In the particle size distribution of sample 4 (Fig. 4(f)), sample 5 (Fig. (c)) and sample 6 (Fig. 5(f)), it is evident that lower fuel concentrations play a crucial role in regulating particle size by influencing the distribution of fuel molecules around the nanoparticles' nuclei. With a decreased amount of fuel, the available

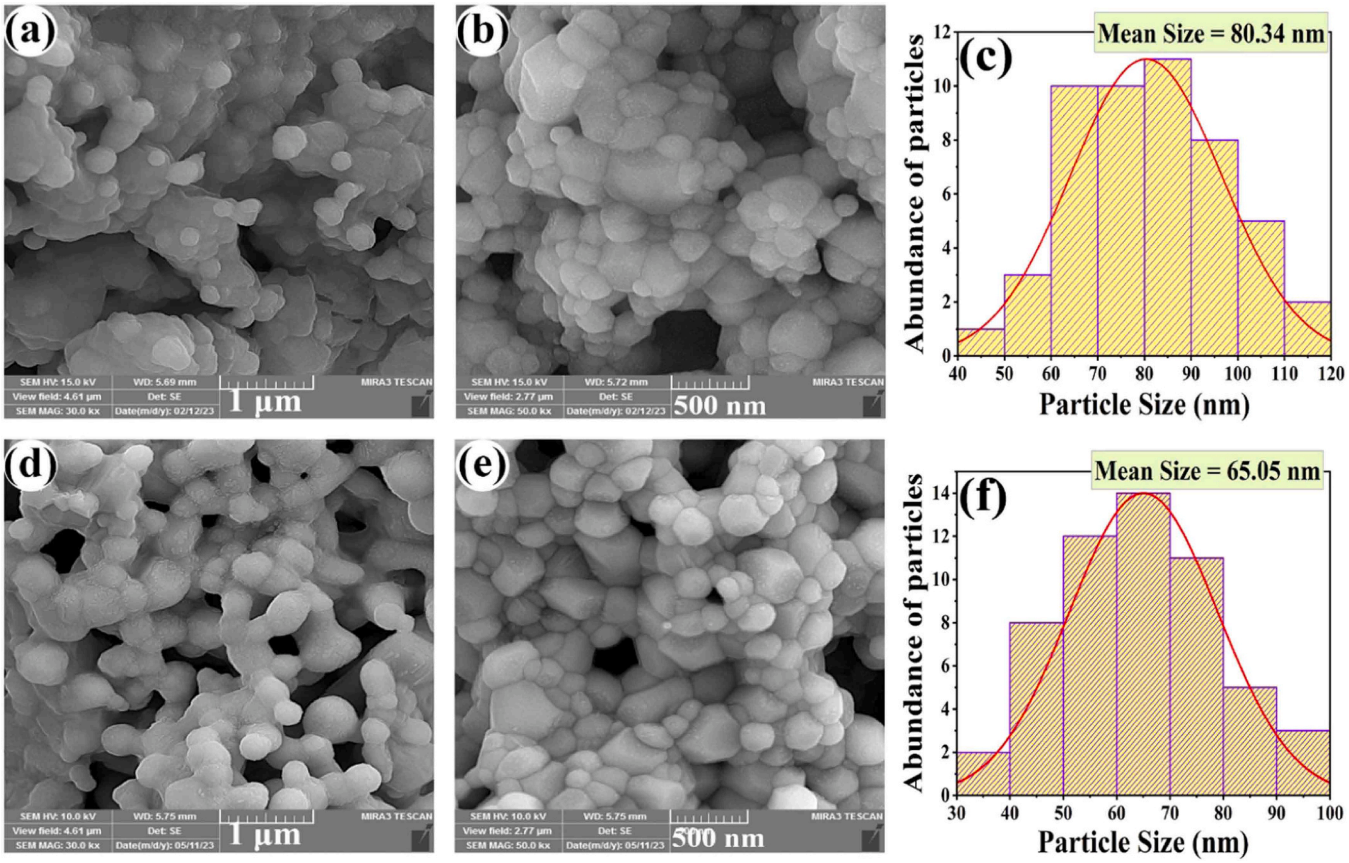

Fig. 4. : SEM images of $SrNiO_3$/NiO nanostructures sample 3 (a) and (b), particle size distribution of sample 3 (c), SEM images of $SrNiO_3$/NiO nanostructures sample 4 (d) and (e), particle size distribution of sample 4 (f).

molecules efficiently encapsulate and stabilize the growing nanoparticles. Consequently, this controlled dispersion of fuel molecules leads to the regulation of the growth process, resulting in the formation of smaller particle sizes. Conversely, higher fuel concentrations lead to the accumulation of an excess of fuel molecules around the nanoparticles, facilitating their agglomeration and subsequent increase in size. This surplus of fuel molecules serves as agents for the aggregation of nanoparticles, causing them to cluster together and produce larger particle sizes. Thus, the concentration of the fuel significantly impacts the size distribution of the nanoparticles. Lower fuel concentrations promote the formation of smaller nanoparticles through controlled dispersion, while higher concentrations induce nanoparticle agglomeration, leading to the production of larger particle sizes. Finally, Sample 7 was prepared as a control without any added fuel. SEM images of this sample are presented in Fig. 5(g) and (h). It is evident that the absence of fuel resulted in the formation of larger particles with a broad and undesirable size distribution (Fig. 5(i)). Based on the combined findings of XRD and SEM, Sample 5 emerged as the most promising candidate for further investigations into the other properties of $SrNiO_3$/NiO/$SrCO_3$ nanocomposites.

In Fig. 6(a), we showcase dark field images of $SrNiO_3$/NiO, offering a closer look at the structural characteristics [46]. Notably, the transmission electron microscopy (TEM) images harmoniously align with the SEM images of sample 5 ((Fig. 5(a) and (b)). These nanostructures exhibit a distinctive spherical morphology, with diameters ranging from 80 to 90 nm. A remarkable feature within the image is the contrast in particle shading, which is indicative of the materials present. The darker particles can be attributed to $SrNiO_3$, while the lighter counterparts are associated with NiO. This clear distinction in contrast helps us distinguish the coexistence of these materials within the nanostructures, providing valuable insights into the composition of $SrNiO_3$/NiO. In Fig. 6(b), high-resolution transmission electron microscopy (HRTEM) images of sample 5 are showcased. The HRTEM analysis reveals precise interplanar distances, notably 0.271 nm corresponding to the (100) lattice plane of SrNiO3 and 0.206 nm attributed to the (200) lattice plane of NiO. However, determination of interplanar distances and Miller indices for $SrCO_3$ is hindered by its less discernible appearance within the particles.

The chemical purity of $SrNiO_3$/NiO/$SrCO_3$ nanocomposites was assessed through EDS analysis. In Fig. 7(a), the EDS spectrum for sample 5 of $SrNiO_3$/NiO nanostructures is presented. This spectrum displays distinct peaks corresponding to the elements Ni, Sr, and O, serving as strong evidence for the chemical purity of the $SrNiO_3$/NiO/$SrCO_3$ nanocomposites. Furthermore, the weight percentages (W%) of each component are in alignment with the expected elemental ratio within $SrNiO_3$/NiO/$SrCO_3$ nanocomposites. Additionally, in Fig. 7(b), the EDS spectrum of sample 1 with high $SrCO_3$ as impurity is shown, and the ratio of elements confirms the composition.

3.3. Surface analysis and magnetic study of $SrNiO_3$/NiO/$SrCO_3$ nanocomposites

The BET analysis is a common technique used to assess the surface characteristics and porosity of materials. Fig. 8 is the nitrogen adsorption–desorption isotherms and pore size profiles of $SrNiO_3$/NiO/$SrCO_3$ nanocomposites sample 5. The BET analysis of $SrNiO_3$/NiO/$SrCO_3$ nanocomposites revealed important surface properties. The specific surface area (SSA) was determined to be 14.75 m^2/g, indicating the available surface area for adsorption. The total pore volume at $P/P_0 = 0.99$ was measured at 5.46×10^{-2} cm^3/g, which signifies the volume of pores within the material. The mean pore diameter was found to be 148.2 nm, indicating the average size of the pores in the nanoparticles.

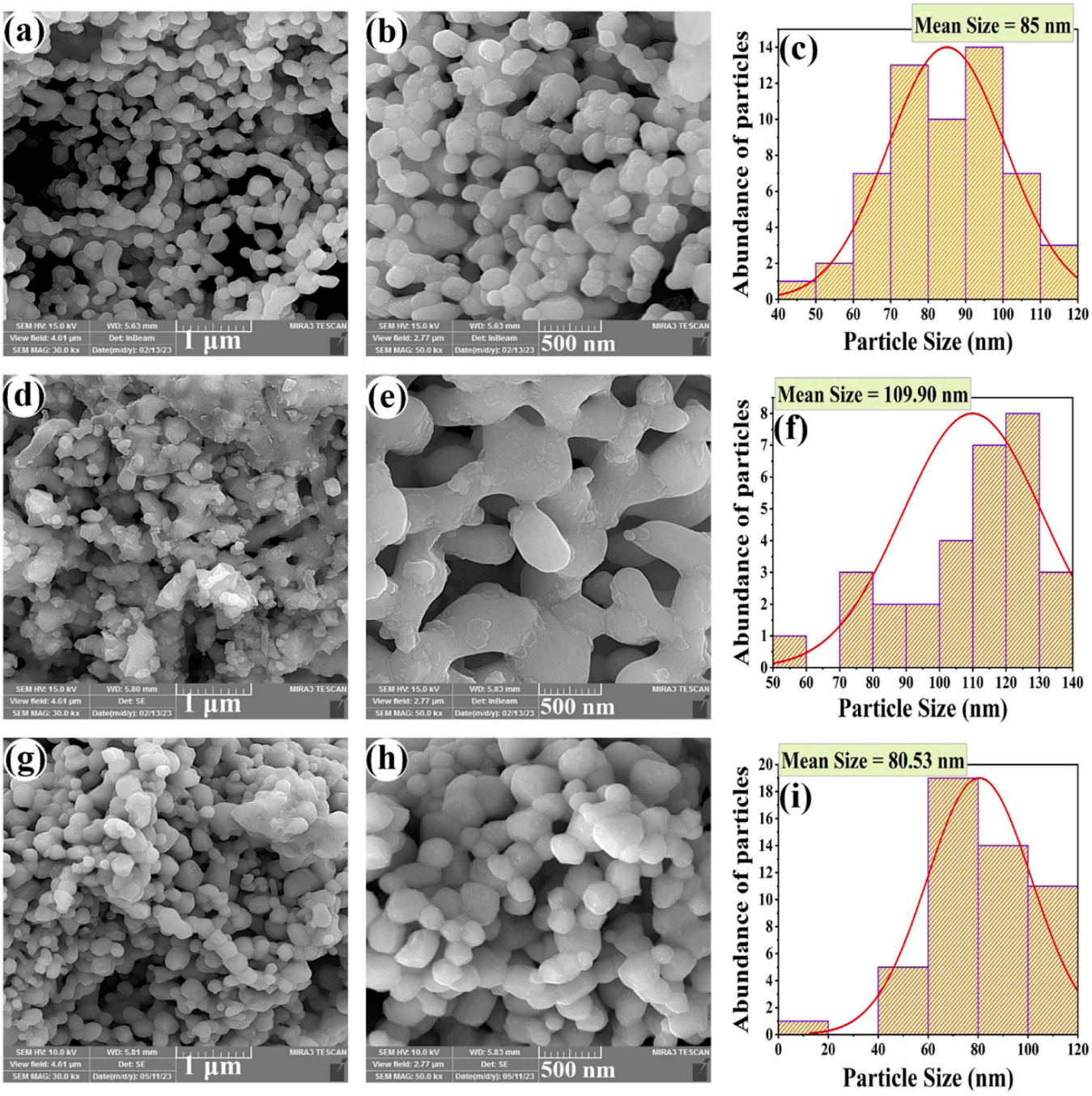

Fig. 5. : SEM images of $SrNiO_3$/NiO nanostructures sample 5 (a) and (b), particle size distribution of sample 5 (c), SEM images of $SrNiO_3$/NiO nanostructures sample 6 (d) and (e), particle size distribution of sample 6 (f) and SEM images of $SrNiO_3$/NiO nanostructures sample 7 (g) and (h), particle size distribution of sample 7 (i).

The nitrogen adsorption/desorption isotherms acquired at −196°C displayed characteristics in line with type IV isotherms as per IUPAC categorization [47]. Furthermore, these isotherms were accompanied by H3 hysteresis loops, which serve as an indicator of well-structured mesoporous materials. Additionally, the BET plot showed a Vm value of 35.52 Va/cm^3 (STP).g^{-1}, indicating the monolayer adsorption volume. The C value, 4.121, might be related to the BET constant. Table 2 provides a more comprehensive description of the BET analysis. In Fig. 8, the observed hysteresis loop is open, indicative of the adsorption-desorption process. Such occurrences can sometimes be attributed to gas trapping in small and undefined holes within the material [48]. However, the classification of this hysteresis loop as H3 suggests a mesoporous structure, facilitating easy gas release.

The limited time allocated for analysis may have contributed to this phenomenon, as a more comprehensive investigation could potentially yield a closed-loop curve. Thus, it is important to note that the time constraints during analysis were a limiting factor in fully elucidating the adsorption behavior of the material.

An investigation was conducted to provide experimental evidence for a particular classification. The chosen approach involved analyzing an optimal sample, known as sample 5, using a VSM (Vibrating Sample Magnetometer). The results obtained, as displayed in Fig. 9, confirmed and validated the weak ferromagnetic characteristics of $SrNiO_3$/NiO/$SrCO_3$ nanocomposites in sample 5. The VSM analysis's spectrum revealed significant magnetic parameters that supported this classification. Specifically, the values for saturation magnetization (Ms),

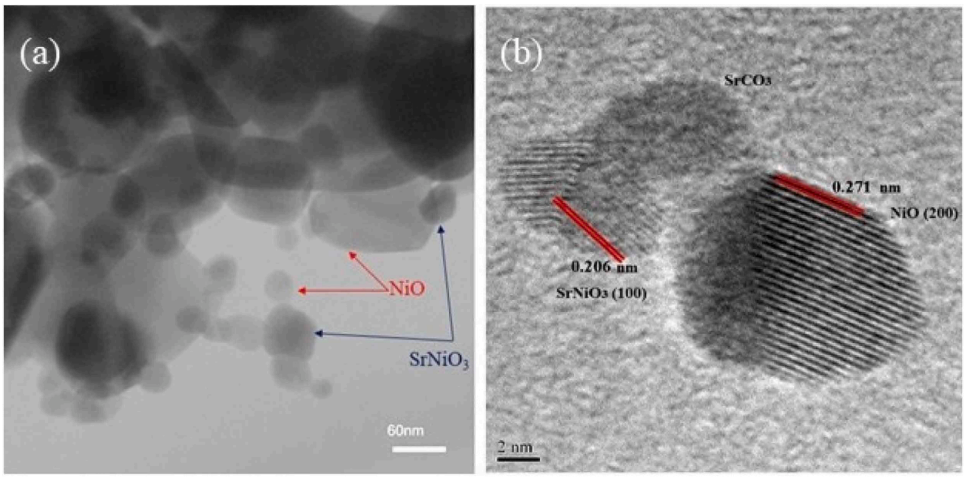

Fig. 6. : (a) TEM image and (b)HRTEM image of $SrNiO_3$/NiO/$SrCO_3$ nanostructures sample 5.

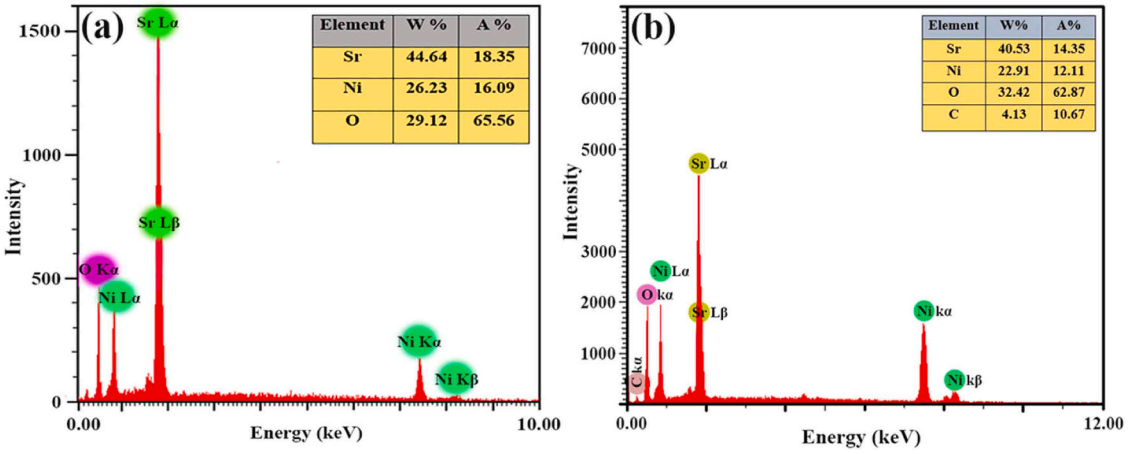

Fig. 7. : EDS spectrum of $SrNiO_3$/NiO nanostructures sample 5 (a) and sample 1 (b).

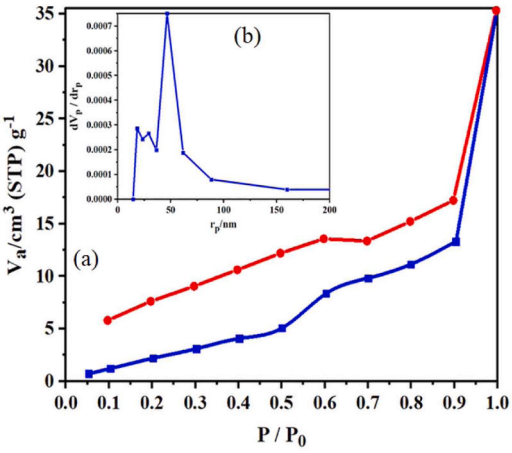

Fig. 8. : N_2 adsorption/desorption isotherms (a) and (b) BJH curves of $SrNiO_3$/NiO nanostructures sample 5.

remnant magnetization (Mr), and coercive field (Hc) were determined as 0.0448 emu/g, 0.11604 emu/g, and 341.9972 Oe, respectively. These numerical values offered quantitative insights into the magnetic behavior of the nanoparticles. Ultimately, these results from the VSM analysis provided experimental validation for the reported ferromagnetic properties of $SrNiO_3$/NiO/$SrCO_3$ nanocomposites, aligning with prior research findings [49,50].

Table 2
BET data of $SrNiO_3$/NiO nanostructures sample 5.

BET plot	Data value	Data unit
V_m	35.52	V_a/Cm^3 (STP).g^{-1}
Specific surface area (SSA)	14.75	$m^2.g^{-1}$
C	4.121	-
Total pore volume ($P/P_0 = 0.99$)	5.46×10^{-2}	$cm^3.g^{-1}$
Mean pore diameter	148.2	nm
BJH plot	**Data value**	**Data unit**
a_p	22.14	$m^2.g^{-1}$
V_p	6.01×10^{-2}	$cm^3.g^{-1}$
r_p (vol)	46.53	nm

3.4. Optical properties of $SrNiO_3$/NiO/$SrCO_3$ nanocomposites

In Fig. 10, the UV absorbance spectrum of $SrNiO_3$/NiO/$SrCO_3$ nanocomposites in sample 5 is depicted, revealing a notable absorbance peak within the range of 580–660 nm. This peak signifies the wavelength at which the material exhibits its highest absorption of light, indicative of its electronic properties. Additionally, the Diffuse Reflectance Spectroscopy (DRS) spectrum provides insights into the band gap of the nanostructure. The DRS spectrum demonstrates that the band gap of $SrNiO_3$/NiO/$SrCO_3$ nanocomposites in sample 5 is measured at 2.5

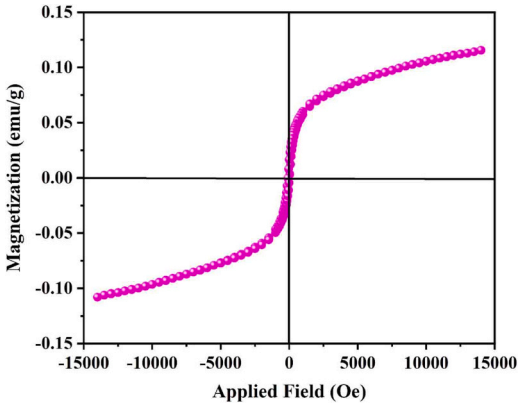

Fig. 9. : VSM spectrum of $SrNiO_3$/NiO nanostructures sample 5.

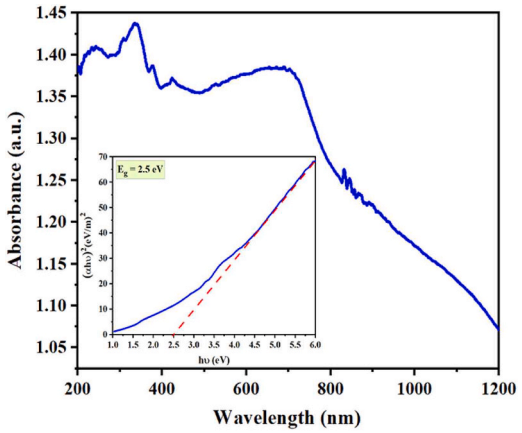

Fig. 10. : UV-Vis (a) and DRS of $SrNiO_3$/NiO nanostructures sample 5 (b).

electron volts (eV). This band gap is a crucial parameter, as it indicates the energy difference between the valence band and the conduction band, which has implications for the material's semiconducting properties and potential applications in electronic devices and photocatalyst. Based on the band gap of 2.5 (eV) observed in the UV absorbance and DRS spectrum of $SrNiO_3$/NiO/$SrCO_3$ nanocomposites in sample 5, it can be inferred that these, as-prepared nanostructures are well-suited for use as photocatalysts in visible light [38]. A band gap of this magnitude falls within the range that allows these materials to effectively harness visible light energy for photocatalytic processes. This characteristic is particularly advantageous for applications such as water purification, pollutant degradation, and solar energy conversion, where visible light is a readily available energy source for catalytic reactions.

The FTIR analysis of $SrNiO_3$/NiO/$SrCO_3$ nanocomposites, prepared by the auto-combustion method, reveals essential insights into the material's chemical composition and structural characteristics in Fig. 11. The identification of five prominent peaks in the spectrum delineates key chemical bonds and potential impurities. Peaks at 524 cm^{-1} and 609 cm^{-1} represent the Ni-O and Sr-O bonds [51,52], confirming the existence of these critical chemical bonds within the material. Furthermore, the peak at 3420 cm^{-1} signifies the stretching vibrations of hydroxyl (OH) groups, indicating the adsorption of water molecules on the sample's surface. Additionally, the presence of $SrCO_3$ as an impurity is evident from peaks observed at 856 cm^{-1}, 1043 cm^{-1}, 1450 cm^{-1}, and 2164 cm^{-1} that attributed to the bending vibrations of carbonate (CO_3^{2-}) ions, stretching vibrations of carbonate (CO_3^{2-}) ions, asymmetric stretching vibrations of CO_3^{2-} ions and stretching vibrations of a triple bond, such as in a cyanide group (C≡N). However, in the context of $SrNiO_3$/NiO, it's less common and might indicate the presence of a

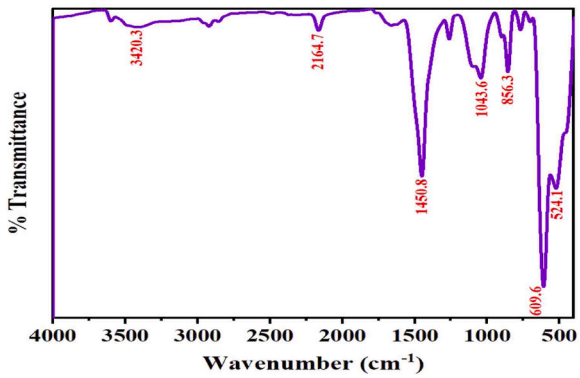

Fig. 11. : FTIR spectrum of $SrNiO_3$/NiO nanostructures sample 5.

unique functional group or impurity.

Through XRD and FTIR analyses, it was observed that the utilization of lactose as a fuel source resulted in a notable reduction in $SrCO_3$ impurities compared to glucose. This improvement can be attributed to the unique chemical properties and decomposition pathways of lactose, which facilitate a more controlled combustion process. Lactose, a disaccharide composed of glucose and galactose, exhibits distinct reactivity during combustion, leading to enhanced control over reaction kinetics and thermodynamics. Consequently, the formation of undesired $SrCO_3$ phases is minimized, ensuring the synthesis of purer $SrNiO_3$/NiO/$SrCO_3$ nanocomposites

4. Photocatalyst performance evaluation

The study investigated the photocatalytic performance of $SrNiO_3$/NiO/$SrCO_3$ nanocomposites when exposed to sunlight, focusing on the degradation of MO MV. Initially, the key parameter under scrutiny was the pollutant concentration. In Fig. 12 (a) and (b), the photocatalyst's performance is depicted, showing the kinetics of MO and MV photodegradation at 20 ppm concentration. Impressively, a consistent rate of degradation was observed, reaching 92 % for MO and 84.8 % for MV after 90 minutes. Fig. 12 (c) to (f) unveil the impact of increasing pollutant concentration on photocatalyst activity. At 25 ppm of MO and MV, the $SrNiO_3$/NiO/$SrCO_3$ nanocomposites demonstrated a slightly weaker performance, achieving yields of 90 % and 82.5 % (Fig. 12 (c) and (d)). Subsequently, in Fig. 12 (e) and (f), the photocatalytic efficiency decreased to 85.4 % and 81.5 % for MO and MV, respectively. This concentration-induced effect on photocatalyst performance can be attributed to several factors. Notably, the increased pollutant concentration reduces the availability of active sites on the photocatalyst's surface, hindering the photodegradation process. Furthermore, factors such as dye aggregation, charge carrier scavenging, and mass transport limitations also contribute to the observed reduction in photocatalyst performance [18,53]. This study highlights the intricate relationship between pollutant concentration and photocatalyst activity, shedding light on the multifaceted factors influencing the degradation of MO and MV in the presence of $SrNiO_3$/NiO/$SrCO_3$ nanocomposites under sunlight.

The impact of $SrNiO_3$/NiO/$SrCO_3$ nanocomposites dosage on photocatalysis was investigated in this study. In Fig. 13 (a) and (b), the photocatalyst plot and reaction kinetics were observed as the nano-catalyst dosage was reduced to 0.03 g. It became evident that decreasing the nano-catalyst dosage had a pronounced effect on the photodegradation performance of MO (79.8 %) and MV (48.8 %), resulting in a noticeable decline in their efficiency. Fig. 13 (c) and (d) illustrate the consequences of further reducing the nano-catalyst dosage to 0.01 g.

At this lower dosage, the $SrNiO_3$/NiO/$SrCO_3$ nanocomposites struggled to exhibit optimal photodegradation performance. The yield

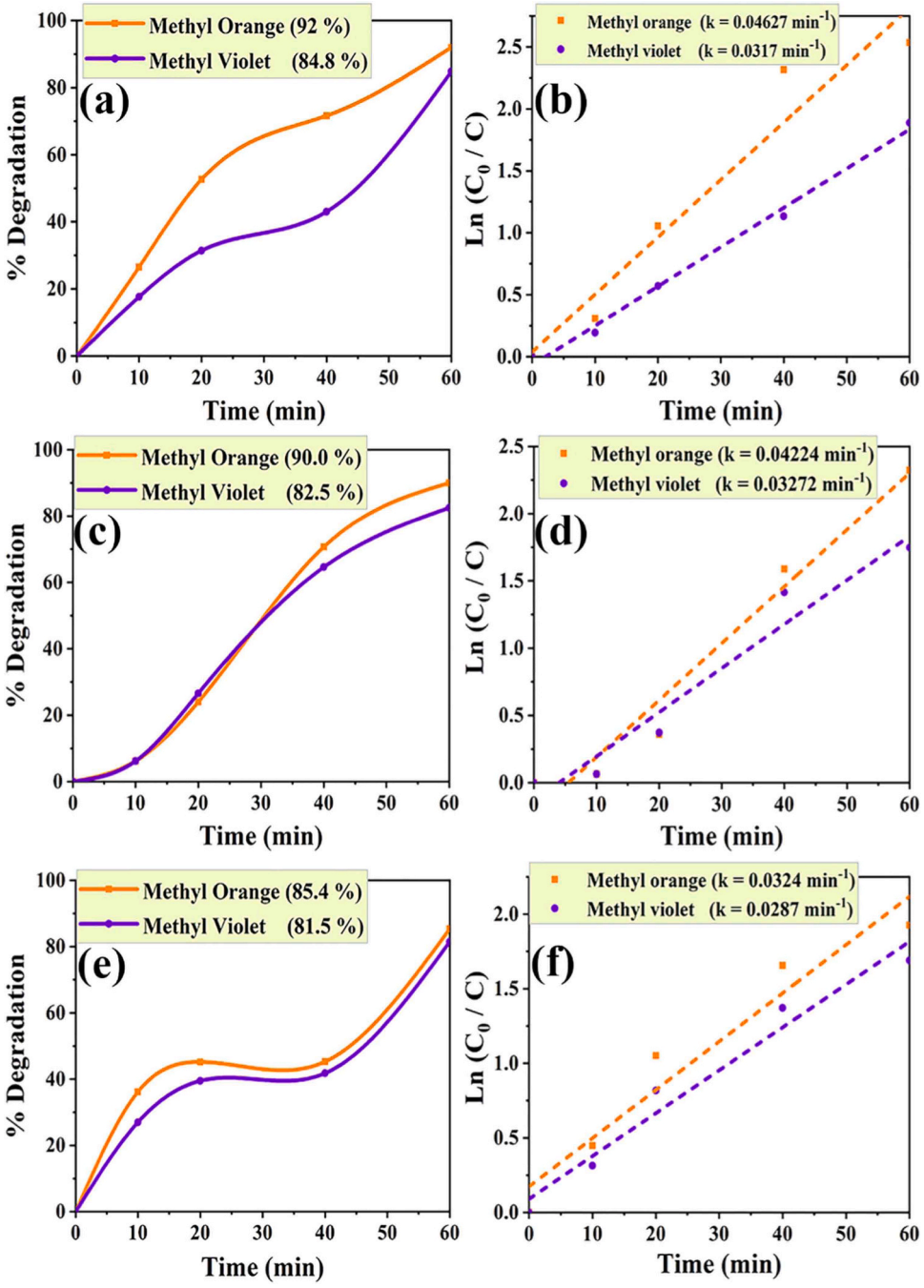

Fig. 12. : Photocatalytic degradation and kinetic reaction profiles of MO and MV at different concentration ((a) and (b) for 20 ppm (c) and (d) for 25 ppm and (e) and (f) for 30 ppm) in the presence of sun-like light using 0.03 g $SrNiO_3$/NiO nanostructures at pH 7.

of the photocatalyst significantly decreased to 16.7 % for MO and 38.2 % for MV degradation. This reduction in photocatalyst yield with decreasing nano-catalyst dosage can be attributed to the limited availability of active sites on the nanostructure's surface. With less nano-catalyst material, fewer active sites are accessible for the photo-degradation of pollutants, ultimately resulting in reduced photocatalytic efficiency. The observed decrease in yield emphasizes the critical role of an appropriate nano-catalyst dosage in achieving efficient photo-degradation of pollutants in the presence of $SrNiO_3$/NiO/$SrCO_3$ nano-composites. Adjusting the dosage is a crucial consideration in optimizing photocatalytic processes for environmental remediation.

The study examined various parameters of the photocatalyst, including pollutant concentration, nanocatalyst dosage, and pH level. The results confirmed that the optimum performance was achieved at a pollutant concentration of 20 ppm, a nanocatalyst dosage of 0.05 g, and a pH of 7. All experiments were conducted under simulated sunlight conditions. Subsequently, the photocatalyst activity of $SrNiO_3$/NiO/$SrCO_3$ nanocomposites was investigated under UV light in these optimized conditions. The results of photo degradation and the kinetic rate of the photocatalyst reaction are presented in Fig. 14(a) and (b). As expected, the use of UV light did affect the photocatalytic efficiency, but the enhancement was not significantly pronounced. This is in line with previous reports, where achieving up to 90 % photodegradation in 60 minutes is considered a remarkable achievement. Specifically, the degradation of MO increased from 92 % to 94 %. In many cases, nano photocatalysts, especially in this family, have shown limited potential in

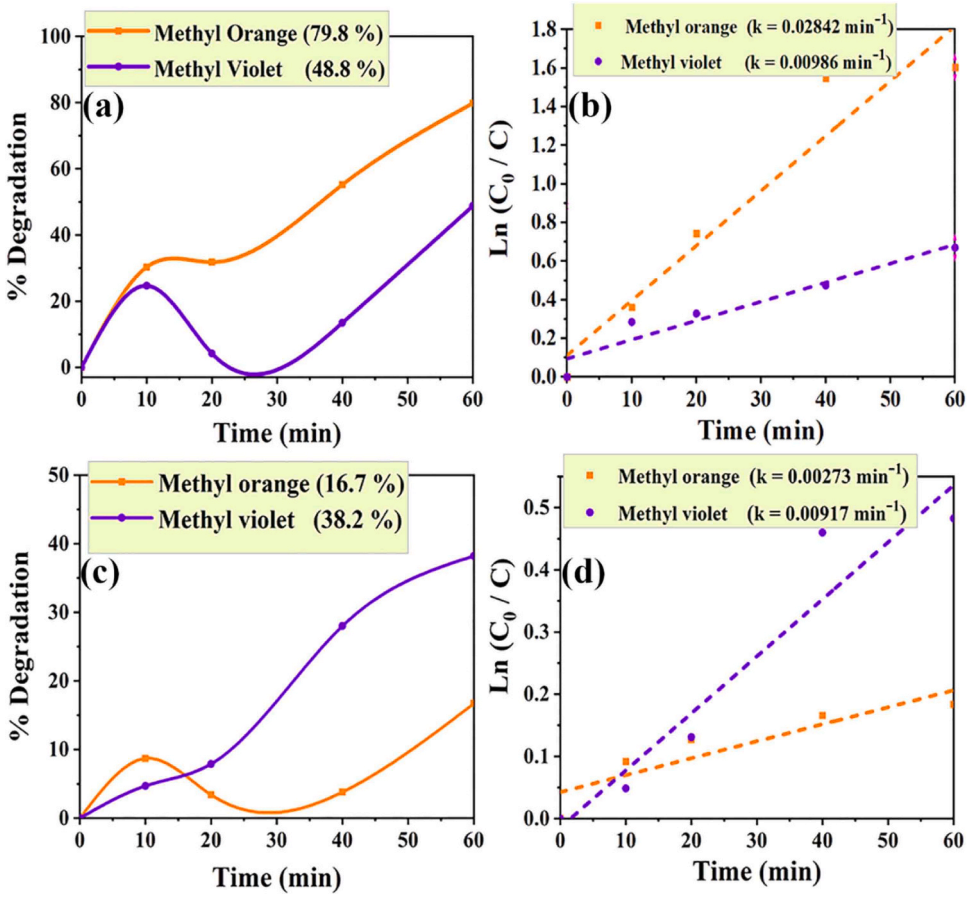

Fig. 13. : Photocatalytic degradation and kinetic reaction profiles of MO and MV at varying nanocatalyst dosages ((a) and (b) for 0.03 g; (c) and (d) for 0.01 g) under Sun-like light using 20 ppm of dye at pH 7.

degrading organic pollutants or have required extended exposure times to reach the desired 90 % photocatalyst degradation level. The influence of solution pH on the photocatalytic performance of $SrNiO_3/NiO/SrCO_3$ nanocomposites has been a critical parameter in our investigation. While all previous photocatalyst experiments were conducted under a neutral pH of 7, we sought to explore the impact of pH variations on photodegradation efficiency. To achieve this, two separate photocatalyst experiments were meticulously executed for each pollutant, one under acidic conditions (pH = 3) achieved through the addition of HCl (0.1 molar), and the other under basic conditions (pH = 11) adjusted with NaOH (0.1 molar). Notably, the acidic environment exerted a profound effect on the photocatalyst's performance, as evidenced in Fig. 14 (c) and (d). Under pH 3, the photocatalyst yield experienced a significant reduction, plummeting to a mere 5 % for MO and 38 % for MV. Conversely, the basic environment at pH 11 did not lead to an enhancement in photodegradation efficiency, as demonstrated in Fig. 14 (c) and (d). In this setting, the photocatalytic activity was observed to be 45 % for MO and 66 % for MV. These results underscore the substantial impact of pH alterations on the efficiency of photocatalytic activities and emphasize the significance of pH regulation in optimizing photocatalyst performance for environmental remediation applications.

The general photocatalyst mechanism for degradation of pollutant provided bellow:

$SrNiO_3/NiO/SrCO_3 + h\nu$ (Visible) → $SrNiO_3/NiO/SrCO_3$ ($e^-_{CB} + h^+_{VB}$)

$SrNiO_3/NiO/SrCO_3$ (h^+_{VB}) + H_2O → ($SrNiO_3/NiO/SrCO_3$)*+ $H^+ + OH^\bullet$

$SrNiO_3/NiO/SrCO_3$ (e^-_{CB}) + O_2 → ($SrNiO_3/NiO/SrCO_3$)* + $O_2^{\bullet-}$

$e^- + O_2 \rightarrow \bullet O_2^-$

$O_2\bullet^- + H^+ \rightarrow HO_2\bullet$

$\bullet O_2^- + H^+ + e^- \rightarrow HOO\bullet$

$HOO\bullet + H_2O \rightarrow \bullet OH + H_2O_2$

$\bullet O_2^- + 2H^+ \rightarrow H_2O_2$

h^+_{VB} + MO or MV → oxidation products

e^-_{CB} + MO or MV → reduction products

$\bullet O_2^-$ + MO or MV (pollutants) → degradation products (H_2O, CO_2)

•OH + MO or MV (pollutants) → degradation products (H_2O, CO_2)

In the photocatalytic degradation process using $SrNiO_3/NiO/SrCO_3$ as the catalyst, the choice of solution acidity plays a crucial role in determining the catalyst's performance. In both acidic and basic solutions, the yield of the photocatalyst is reduced. In acidic conditions, the abundance of H^+ ions can competitively react with the photoexcited state (h^+_{VB}), limiting its availability for the desired oxidation reactions. Meanwhile, basic solutions with an excess of OH^- ions tend to react with the photoexcited state (e^-_{CB}), hindering the generation of electron-hole pairs necessary for the photocatalytic process. However, the photocatalyst demonstrates its best performance at a pH of 7, which is a neutral environment. At this pH level, the concentration of H^+ and OH^- ions is balanced, minimizing their interference and maintaining the availability of both h^+_{VB} and e^-_{CB} states. This equilibrium promotes efficient electron-hole pair generation and subsequent reactions, making pH 7 the optimal condition for the photocatalyst to efficiently degrade

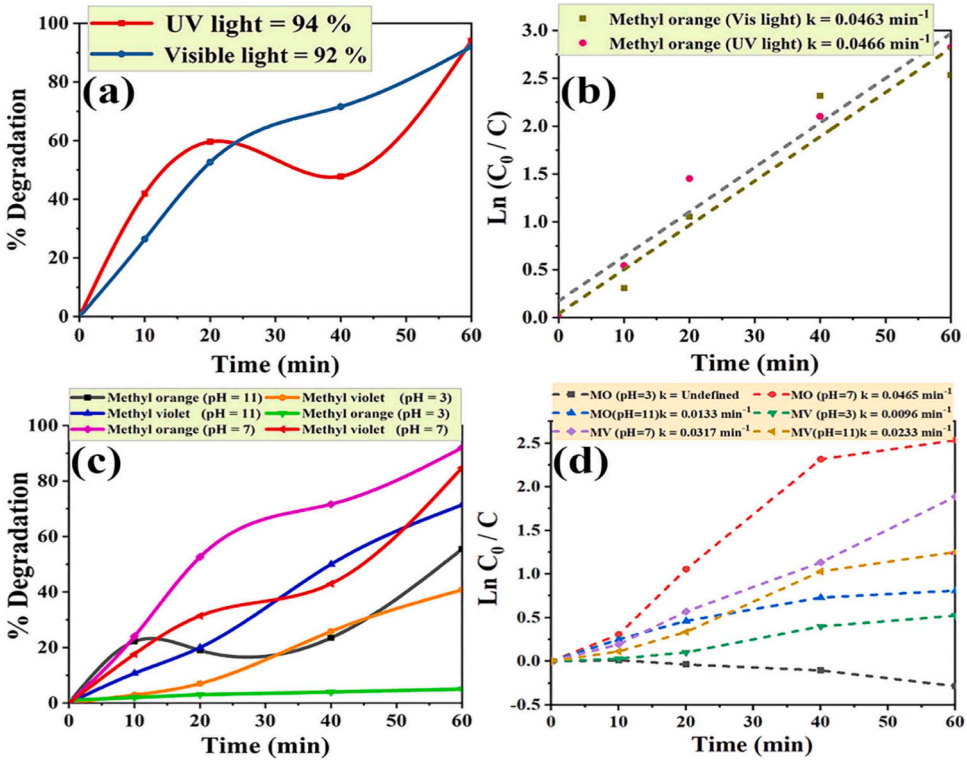

Fig. 14. : Photocatalytic degradation and kinetic reaction profiles of MO in the presence of $SrNiO_3/NiO/SrCO_3$ nanostructures under UV and sun-like light conditions (a) and (b), and photocatalytic degradation and kinetic reactions of MO and MV under sun-like light at different pH levels (c) and (d).

pollutants and yield the best results. When adjusting the pH of the solution for photocatalytic experiments, hydrochloric acid was employed as a pH modifier. The choice of pH adjustment is crucial for optimizing the performance of photocatalysts, especially those involving $SrNiO_3/NiO/SrCO_3$ nanocomposites nanocomposites. However, it's essential to consider the potential interactions between the acid and alkaline oxides present in the catalyst. Hydrochloric acid, being a strong acid, readily dissociates into H^+ and Cl^- ions in solution. These H^+ ions may react with alkaline oxides, such as nickel oxide (NiO) and strontium carbonate ($SrCO_3$), which are components of the $SrNiO_3/NiO/SrCO_3$

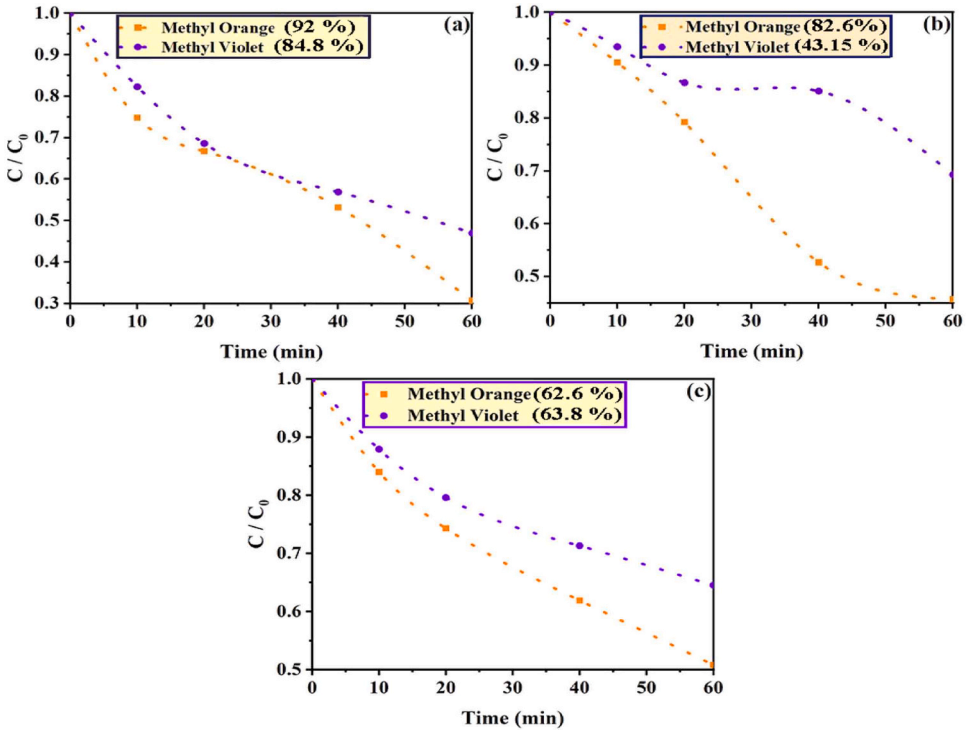

Fig. 15. : Photocatalyst plot and Kinetics study of $SrNiO_3/NiO/SrCO_3$ nanocomposite (sample 5) (a), NiO (b) and $SrNiO_3/NiO/SrCO_3$ nanocomposite (sample 1) (c).

nanocomposites. This reaction could potentially lead to the formation of water and corresponding salts, thereby altering the composition and surface properties of the catalyst. The reactivity of hydrochloric acid with alkaline oxides may result in catalyst deactivation or modification, affecting its photocatalytic performance. For instance, the formation of new compounds or surface species could interfere with the generation of electron-hole pairs or alter the catalyst's surface chemistry, ultimately impacting its ability to degrade organic pollutants. While significant catalyst deactivation was not observed under the experimental conditions, future studies may explore alternative pH adjustment methods to mitigate potential reactions with alkaline oxides. Techniques such as using buffered solutions or adjusting pH gradually with weaker acids may help minimize unwanted interactions while maintaining optimal pH conditions for photocatalysis.

Also, in order to comparing the photocatalytic activity of different samples, experiments were conducted to assess the degradation efficiency of MO and MV under visible light irradiation. Sample 5, featuring a high percentage of $SrNiO_3$, and sample 1, with a high percentage of $SrCO_3$, were compared alongside pure NiO. The degradation percentages, as depicted in Fig. 15 through the C/C_0 plots, illustrate distinct variations among the samples. Sample 5 demonstrated superior photocatalytic performance, achieving degradation percentages of 92 % for MO and 84.8 % for MV. Conversely, pure NiO exhibited lower efficiencies, recording values of 82.6 % for MO and 43.15 % for MV. Similarly, sample 1, characterized by a higher $SrCO_3$ content, displayed degradation efficiencies of 62.6 % for MO and 63.8 % for MV.

These findings underscore the significant impact of material composition on photocatalytic activity under visible light irradiation, with sample 5, enriched with $SrNiO_3$, emerging as the most effective catalyst among the tested samples. For instance, in 2010, Li et al. reported that $LaNiO_3$, prepared using the sol gel combustion method, had a 2.26 eV band gap and could achieve 74.9 % efficiency in degrading MO during a 300-minute visible light radiation [54]. Another study evaluated the photocatalyst activity of $LaNiO_3/TiO_2$ for the degradation of MO, conducted by Chen et al. Their research group reported a 58 % photocatalyst yield during a 75-minute period of visible light exposure [55]. In 2022, C. Maridevaru et al. synthesized $CeNiO_3$ nanoparticles using the hydrothermal method and studied their photocatalyst activity in degrading Orang G (OG) [56]. As they reported, $CeNiO_3$ was able to degrade OG in the presence of UV light over 240 minutes. Comparing this study to similar previous works, it becomes evident that the $SrNiO_3/NiO/SrCO_3$ nanocomposites employed in this research yielded highly valuable results in the photodegradation of organic pollutants. To facilitate this comparison with other reports, Table 3 has been provided.

As part of this study, we investigated the effectiveness of $SrNiO_3/NiO/SrCO_3$ nanocomposites as photocatalysts for the degradation of Methyl orange, a common environmental pollutant, using $SrNiO_3/NiO/SrCO_3$ nanocomposites as photocatalysts. To ascertain the primary radicals involved in the photocatalytic process, various radical scavengers employed in the experimental setup. As depicted in Fig. 16 (a), the addition of ethylenediaminetetraacetic acid (EDTA) to the reaction mixture resulted in a noticeable decrease in photocatalyst performance, with the degradation efficiency dropping from 92 % to 80.8 %. Similarly, the introduction of benzoic acid as a scavenger led to a further reduction in performance, yielding a degradation efficiency of 68.7 %. Notably, the inclusion of benzoquinone as a scavenger had a profound impact, causing a significant decline in photocatalyst activity, reducing the efficiency from 92 % to 35.5 %. This compelling evidence strongly suggests that the primary radical responsible for the degradation of Methyl orange in our system is the superoxide radical ($O_2^{\bullet -}$). These findings provide valuable insights into the mechanistic aspects of photocatalytic pollutant degradation when employing $SrNiO_3/NiO/SrCO_3$ nanocomposites as the catalyst, underscoring the pivotal role of $O_2^{\bullet -}$ radicals in this photocatalytic process.

The stability of photocatalysts is a pivotal factor in assessing their practical applicability for environmental remediation processes. In our investigation of the stability of $SrNiO_3/NiO/SrCO_3$ nanocomposites as photocatalysts, we conducted a comprehensive study involving five consecutive photocatalytic rounds. After each round, the nanostructures were meticulously separated via centrifugation, collected, and subjected to a controlled drying process at 60 °C. The findings, as depicted in Fig. 16 (b), revealed a progressive reduction in photocatalyst performance as the photocatalytic cycles advanced. Specifically, the initial photocatalytic efficiency of 92 % experienced a modest decrease to 86.2 % in the second round, signifying a slight decline in performance. However, as the cycles continued, a more pronounced deterioration was observed, with photocatalytic efficiencies of 74.5 %, 67.4 %, and 60.1 % recorded for the third, fourth, and fifth rounds, respectively. These results underscore the importance of evaluating the stability of $SrNiO_3/NiO/SrCO_3$ photocatalysts over multiple operational cycles. The observed performance decline may be attributed to a variety of factors, including catalyst deactivation, aggregation, or structural changes, necessitating further investigation to elucidate the underlying mechanisms and refine the catalyst's long-term performance for practical environmental remediation applications.

A comprehensive analysis of the energy band structures within composite semiconductor materials is imperative for elucidating their photocatalytic mechanisms. In this context, the relative band positions of constituent semiconductors, such as $SrNiO_3$, NiO, and $SrCO_3$, were meticulously investigated. Utilizing Mulliken electronegativity theory, as delineated by [57], enabled the prediction of conduction band edge (ECB) and valence band edge (EVB) positions for these composite materials. Drawing from these theoretical frameworks, a putative charge transfer mechanism reminiscent of a type-I heterojunction was postulated for $SrNiO_3/NiO/SrCO_3$ nanocomposites, with potential implications for methylene blue (MB) degradation. Calculations revealed EVB values ranging from 0.32 eV to 1.78 eV for pristine $SrNiO_3$ and from 0.547 eV to 3.05 eV for NiO nanostructures, referenced relative to the

Table 3
Photocatalyst conditions and results.

Name of dye	Concentration (ppm)	Dosage of catalyst (g)	pH	Time / aeration (min)	Degradation (%)
Methyl orange	20	0.05	7	60 / 30	92
Methyl orange	25	0.05	7	60 / 30	90
Methyl orange	30	0.05	7	60 / 30	85.4
Methyl orange (optimum)	20	0.03	7	60 / 30	79.8
Methyl orange (optimum)	20	0.01	7	60 / 30	16.7
Methyl orange (optimum)	20	0.05	3	60 / 30	No response
Methyl orange (optimum)	20	0.05	11	60 / 30	55.5
Methyl violet	20	0.05	7	60 / 30	84.8
Methyl violet	25	0.05	7	60 / 30	82.5
Methyl violet	30	0.05	7	60 / 30	81.5
Methyl violet (optimum)	20	0.03	7	60 / 30	48.8
Methyl violet (optimum)	20	0.01	7	60 / 30	38.2
Methyl violet (optimum)	20	0.05	3	60 / 30	40.7
Methyl violet (optimum)	20	0.05	11	60 / 30	71.4

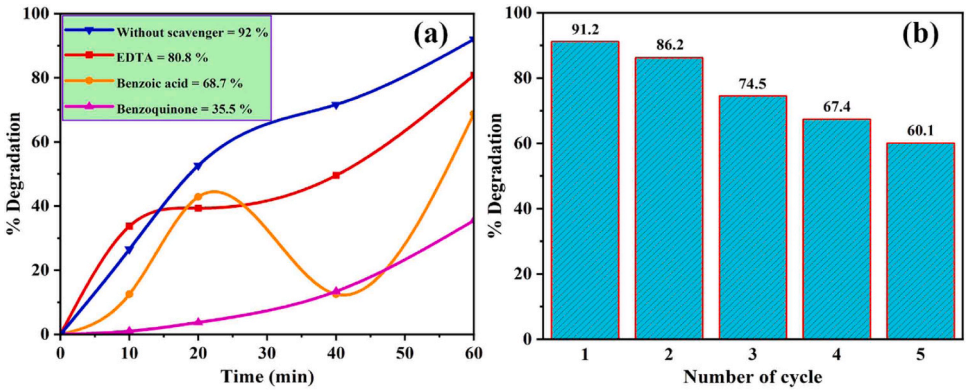

Fig. 16. : Photocatalytic degradation in presence of different scavengers (a) and recycle ability of $SrNiO_3/NiO/SrCO_3$ nanostructures in 5 cycles (b).

normal hydrogen electrode (NHE). Similarly, ECB values for $SrNiO_3$ and NiO nanostructures were estimated within the range of −0.125 eV to −3.04 eV and from 0.547 eV to 3.05 eV, respectively, also referenced to NHE (Fig. 17). Notably, the energy levels of NiO were observed to be enveloped within the wider bandgap of $SrNiO_3$. The conceptualized mechanism for $SrNiO_3/NiO/SrCO_3$ heterojunctions revolves around the effective separation of photo-generated electron-hole pairs, facilitated by facile charge transfer from semiconductor II (NiO) to the conduction and valence bands of semiconductor I ($SrNiO_3$), exploiting the narrower band gap of $SrNiO_3$. Although charge carriers may primarily accumulate at the surface of semiconductor I, the differential recombination rates between charge carriers emerge as a pivotal determinant of degradation efficiency, echoing previous research findings (Table 4). These insights underscore the critical importance of comprehending the energy band alignments within composite materials, offering valuable insights into the intricate mechanisms governing their photocatalytic behavior.

Table 4
Comparison of photocatalytic activity with similar works.

Type of catalyst	Type of dye	Degradation Efficiency	Time (min)	Light Source	Reference
$SrNiO_3$/ NiO/ $SrCO_3$	MO & MV	92 %, 84.8 %	60	Vis	This work
$NdCoO_3$	Malachite green	79.7 %	120	Vis	[58]
$LaNiO_3$	MO	74.9 %	300	Vis	[59]
$BiMnO_3$	Rhodamine B	90 %	55	Vis	[60]
$BaFeO_3$	MO	92 %	120	UV	[61]
$DyCoO_3$	Malachite green	48 %	120	UV	[62]
$DyMnO_3$	MO	85 %	120	UV	[63]
$CeNiO_3$	Orange-G (OG)	73.63 %	240	UV	[64]
$LaNiO_3$/ TiO_2	MO	58 %	75	Vis	[55]
$SrNiO_3$	Acid red	98 %	300	Vis	[65]

5. Conclusion

The main objective of this study was the successful synthesis of $SrNiO_3/NiO/SrCO_3$ nanocomposites through the use of the auto-combustion method. Control over the engineered morphology, size, and purity was achieved through a meticulous manipulation of reaction conditions, including the choice and ratio of fuel and the calcination temperature. $SrNiO_3/NiO/SrCO_3$ nanocomposites of a uniform round shape, measuring between 60 and 70 nm, were obtained by using maltose as fuel in a 2:1 ratio with Sar salt, followed by calcination at

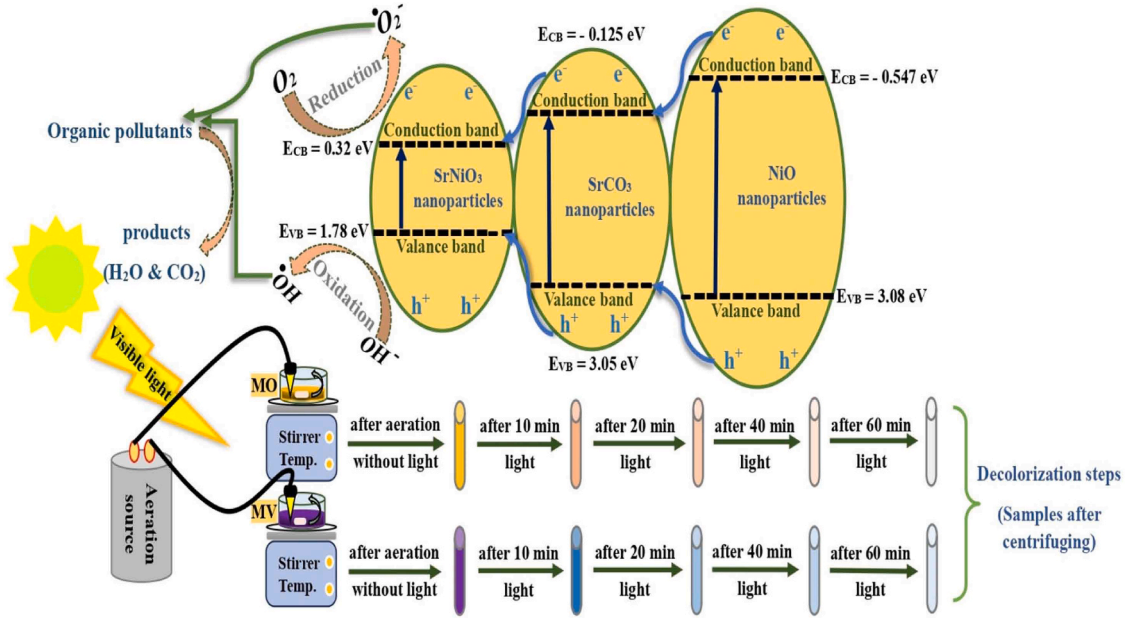

Fig. 17. : Schematic diagram of photocatalytic reaction in the presence of $SrNiO_3/NiO/SrCO_3$ nanocomposites under visible light.

900°C for five hours. Analytical techniques such as XRD, EDS, and FTIR were used to rigorously confirm the purity of the product. Moreover, the VSM spectrum conclusively established that the $SrNiO_3/NiO/SrCO_3$ nanostructures exhibited ferromagnetic properties, with their band gap determined by DRS spectroscopy at an optimal value of 2.6 eV, making them highly suitable for photocatalytic applications. As far as the photocatalysis is concerned, the $SrNiO_3/NiO/SrCO_3$ nanocomposites have been rigorously tested under a variety of parameters, including the concentration of pollutants, the dosage of nanostructures, and the pH level. The nanostructures showed their best photocatalytic performance when subjected to a 20 ppm Methyl orange solution, a dosage of 0.03 g of nanostructures, and a pH of 7. It was found that when natural sunlight is irradiated for 60 minutes, they were able to achieve exceptional levels of pollutant degradation, with a 92 % removal efficiency for Methyl orange and an impressive 84.8 % for the remaining pollutants. As a result, these results outperform those of many other commonly used photocatalysts. Moreover, the investigation into the degradation mechanism revealed that the main reactive radical responsible for pollutant removal was O2•. The nanostructures exhibited remarkable stability, retaining 60.1 % of their photocatalytic activity even after five experiment cycles. This level of durability bodes well for their practical applications in addressing environmental pollution challenges.

CRediT authorship contribution statement

Mojgan Goudarzi: Data curation, Project administration, Resources, Software, Validation, Visualization, Writing – original draft, Writing – review & editing. **Seyed Amirhosein Ehsanzade:** Formal analysis, Investigation, Methodology, Software. **Aseel M. Aljeboree:** Software, Writing – review & editing. **Forat H. Alsultany:** Data curation, Software, Writing – review & editing. **Masoud Salavati-Niasari:** Conceptualization, Data curation, Formal analysis, Funding acquisition, Investigation, Methodology, Project administration, Resources, Software, Supervision, Validation, Visualization, Writing – original draft, Writing – review & editing. **Elmuez A. Dawi:** Resources, Software, Writing – review & editing.

Declaration of Competing Interest

The authors declare that there are no conflicts of interest regarding the publication of this manuscript.

Acknowledgments

Authors are grateful to the council of Iran National Science Foundation (INSF, 97017837) and University of Kashan for supporting this work by Grant No (159271/SAHE1).

References

[1] P. Kumari, M. Alam, W.A. Siddiqi, Usage of nanoparticles as adsorbents for waste water treatment: an emerging trend, Sustain. Mater. Technol. 22 (2019) e00128.
[2] S. Shukla, R. Khan, A. Daverey, Synthesis and characterization of magnetic nanoparticles, and their applications in wastewater treatment: A review, Environ. Technol. Innov. 24 (2021) 101924.
[3] S. Singh, V. Kumar, R. Romero, K. Sharma, J. Singh, Applications of nanoparticles in wastewater treatment, Nanobiotechnology Bioformulations (2019) 395–418.
[4] R. Kalia, A. Chauhan, R. Verma, M. Sharma, K.M. Batoo, R. Kumar, S. Hussain, S. Ghotekar, M.F. Ijaz, Photocatalytic degradation properties of Li-Cr ions substituted CoFe2O4 nanoparticles for wastewater treatment application, Phys. Status Solidi (a) 219 (2022) 2100539.
[5] M. Goudarzi, N. Mir, O. Amiri, M. Salavati-Niasari, Photocatalytic degradation of antibiotic using Ni-doped thallium(I) orthotungstate nanorods: hydrothermal synthesis and characterization, J. Alloy. Compd. 874 (2021) 159856.
[6] M. Goudarzi, M. Salavati-Niasari, S.M. Hosseinpour-Mashkani, N. Mir, Controlled synthesis of Tl 2 O 3 nanostructures via microwave route by a novel pH adjuster and investigation of its photocatalytic activity, J. Mater. Sci.: Mater. Electron. 26 (2015) 5326–5334.
[7] G. Iervolino, I. Zammit, V. Vaiano, L. Rizzo, Limitations and prospects for wastewater treatment by UV and visible-light-active heterogeneous photocatalysis: a critical review, Heterog. Photocatal.: Recent Adv. (2020) 225–264.
[8] S. Royer, D. Duprez, F. Can, X. Courtois, C. Batiot-Dupeyrat, S. Laassiri, H. Alamdari, Perovskites as substitutes of noble metals for heterogeneous catalysis: dream or reality, Chem. Rev. 114 (2014) 10292–10368.
[9] G. Mamba, P.J. Mafa, V. Muthuraj, A. Mashayekh-Salehi, S. Royer, T.I. T. Nkambule, S. Rtimi, Heterogeneous advanced oxidation processes over stoichiometric ABO3 perovskite nanostructures, Mater. Today Nano 18 (2022) 100184.
[10] Z.N. Garba, W. Zhou, M. Zhang, Z. Yuan, A review on the preparation, characterization and potential application of perovskites as adsorbents for wastewater treatment, Chemosphere 244 (2020) 125474.
[11] R. Ji, J. Chen, T. Liu, X. Zhou, Y. Zhang, Critical review of perovskites-based advanced oxidation processes for wastewater treatment: Operational parameters, reaction mechanisms, and prospects, Chin. Chem. Lett. 33 (2022) 643–652.
[12] G.A. Samara, The relaxational properties of compositionally disordered ABO3 perovskites, J. Phys.: Condens. Matter 15 (2003) R367.
[13] J. Romao, G. Mul, Substrate specificity in photocatalytic degradation of mixtures of organic contaminants in water, ACS Catal. 6 (2016) 1254–1262.
[14] P. de Abreu, E.L. Pereira, C.M.M. Campos, F.L. Naves, Photocatalytic Oxidation Process (UV/H 2 O 2/ZnO) in the treatment and sterilization of dairy wastewater, Acta Scientiarum, Technology 35 (2013) 75–81.
[15] F.C. Kent, K.R. Montreuil, R.M. Brookman, R. Sanderson, J.R. Dahn, G.A. Gagnon, Photocatalytic oxidation of DBP precursors using UV with suspended and fixed TiO2, Water Res. 45 (2011) 6173–6180.
[16] Y. Zhang, Y. Wang, D. Zhao, B. Wang, L. Pu, M. Fan, X. Liang, Y. Yin, Z. Hu, X. Yan, Visible light in situ driven electron accumulation at the Ti–Mn–O 3 sites of TiO 2 hollow spheres for photocatalytic hydrogen production, N. J. Chem. 46 (2022) 15443–15450.
[17] Z. Hu, Y. Zhang, Y. Wang, J. Huang, S. Yang, H. Li, Regulation of oriented NO photooxidation to circumvent NO2 with high-coordinated M–N5 (M= Fe, Co, Mn, Ti) sites and far–carbon defects, Appl. Catal. B: Environ. Energy 350 (2024) 123948.
[18] A. Taifi, O.K.A. Alkadir, A.A. Oda, A.M. Aljeboree, A.L. Al Bayaa, A.F. Alkaim, S. A. Abed, Biosorption by Environmental, Natural and Acid-Activated Orange Peels as Low-Cost Aadsorbent: Optimization of Disperse Blue 183 as a Model, IOP Conf. Ser.: Earth Environ. Sci. 1029 (2022) 012009.
[19] M.A. Mahdi, A.M. Aljeboree, L.S. Jasim, A.F. Alkaim, Synthesis, characterization and adsorption studies of a graphene oxide/polyacrylic acid nanocomposite hydrogel, NeuroQuantology 19 (2021) 46–54.
[20] H. Liu, C. Wang, G. Wang, Photocatalytic advanced oxidation processes for water treatment: recent advances and perspective, Chem. – Asian J. 15 (2020) 3239–3253.
[21] B. Wang, X. Guo, Y. Zhang, Y. Wang, G. Huang, H. Chao, W. Wang, Z. Hu, X. Yan, Extraordinary promotion of visible-light hydrogen evolution for graphitic carbon nitride by introduction of accumulated electron sites (BN2), ACS Appl. Energy Mater. 5 (2022) 7479–7489.
[22] Y. Xue, M. Kamali, X. Zhang, N. Askari, C. De Preter, L. Appels, R. Dewil, Immobilization of photocatalytic materials for (waste) water treatment using 3D printing technology–advances and challenges, Environ. Pollut. 316 (2023) 120549.
[23] D. Kanakaraju, F.D. anak Kutiang, Y.C. Lim, P.S. Goh, Recent progress of Ag/TiO2 photocatalyst for wastewater treatment: Doping, co-doping, and green materials functionalization, Appl. Mater. Today 27 (2022) 101500.
[24] A.M. Aljeboree, R.A. Mohammed, M.A. Mahdi, L.S. Jasim, A.F. Alkaim, Synthesis, characterization of P (CH/AA-co-AM) and adsorptive removal of Pb (II) ions from aqueous solution: thermodynamic study, NeuroQuantology 19 (2021) 137–143.
[25] J. Zhang, M. Yang, H. Zhong, M. Liu, Q. Sui, L. Zheng, J. Tong, Y. Wei, Deciphering the factors influencing the discrepant fate of antibiotic resistance genes in sludge and water phases during municipal wastewater treatment, Bioresour. Technol. 265 (2018) 310–319.
[26] R. Mailler, J. Gasperi, Y. Coquet, C. Derome, A. Buleté, E. Vulliet, A. Bressy, G. Varrault, G. Chebbo, V. Rocher, Removal of emerging micropollutants from wastewater by activated carbon adsorption: Experimental study of different activated carbons and factors influencing the adsorption of micropollutants in wastewater, J. Environ. Chem. Eng. 4 (2016) 1102–1109.
[27] Safaa H. Ganduh, Kmal, Q. Rafid, Mahdi, A. Makarim, Aljeboree, M. Aseel, Jasim, S. Layth, Selective spectrophotometric determination of 4-amino antipyrine antibiotics in pure forms and their pharmaceutical formulations, Int. J. Drug Deliv. Technol. 11 (2) (2021) 371–375.
[28] N. Wei, H. Cui, Q. Song, L. Zhang, X. Song, K. Wang, Y. Zhang, J. Li, J. Wen, J. Tian, Ag2O nanoparticle/TiO2 nanobelt heterostructures with remarkable photo-response and photocatalytic properties under UV, visible and near-infrared irradiation, Appl. Catal. B: Environ. 198 (2016) 83–90.
[29] T. Liu, Y. Zhang, Z. Shi, W. Cao, L. Zhang, J. Liu, Z. Chen, BiOBr/Ag/AgBr heterojunctions decorated carbon fiber cloth with broad-spectral photoresponse as filter-membrane-shaped photocatalyst for the efficient purification of flowing wastewater, J. Colloid Interface Sci. 587 (2021) 633–643.
[30] M. Faisal, M. Jalalah, F.A. Harraz, A.M. El-Toni, J.P. Labis, M. Al-Assiri, A novel Ag/PANI/ZnTiO3 ternary nanocomposite as a highly efficient visible-light-driven photocatalyst, Sep. Purif. Technol. 256 (2021) 117847.
[31] C.-W. Siao, W.-L.W. Lee, Y.-M. Dai, W.-H. Chung, J.-T. Hung, P.-H. Huang, W.-Y. Lin, C.-C. Chen, BiOxCly/BiOmBrn/BiOpIq/GO quaternary composites: syntheses and application of visible-light-driven photocatalytic activities, J. Colloid Interface Sci. 544 (2019) 25–36.
[32] S. MSP, M.M. Hossain, G. Gnanasekaran, Y.S. Mok, Dry reforming of propane over γ-Al2O3 and nickel foam supported novel SrNiO3 perovskite catalyst, Catalysts 9 (2019) 68.

[33] T. Nikbeen, A.K. Nayab, Transformation of Traditional Wastewater Treatment Methods into Advanced Oxidation Processes and the Role of Ozonation, J. Ecol. Eng. 24 (2023) 173–189.
[34] J. Junita, D. Jayalakshmi, J.D. Rodney, Effect of annealing temperature on the bifunctional electrocatalytic properties of strontium nickelate (SrNiO3) nanoparticles for efficient overall water splitting, Int. J. Hydrog. Energy 47 (2022) 30602–30612.
[35] X. Wang, Preparation of perovskite type SrNiO3 photocatalyst material by microwave heating method, Adv. Mater. Res. 826 (2013) 211–214.
[36] J. Irvine, J.L. Rupp, G. Liu, X. Xu, S. Haile, X. Qian, A. Snyder, R. Freer, D. Ekren, S. Skinner, Roadmap on inorganic perovskites for energy applications, J. Phys.: Energy 3 (2021) 031502.
[37] N. Ahmad, F. Alharthi, M. Alam, R. Wahab, S. Manoharadas, B. Alrayes, Syngas production via CO2 reforming of methane over SrNiO3 and CeNiO3 perovskites, Energies 14 (2021) 2928.
[38] H. Boucheloukh, K. Harrouche, B. Boughrara, T. Sehili, SrNiO3 perovskite synthesis for enhanced photodegradation of the nonsteroidal anti-inflammatory drug naproxen: a clean and sustainable process for water treatment, Inorg. Chem. Commun. (2023) 111459.
[39] A. Aljuaid, M. Almehmadi, A.A. Alsaiari, M. Allahyani, O. Abdulaziz, A. Alsharif, J. A. Alsaiari, M. Saih, R.T. Alotaibi, I. Khan, g-C3N4 Based Photocatalyst for the Efficient Photodegradation of Toxic Methyl Orange Dye: Recent Modifications and Future Perspectives, Molecules 28 (2023) 3199.
[40] M.Y.A. Khan, M. Zahoor, A. Shaheen, N. Jamil, M.I. Arshad, S.Z. Bajwa, N.A. Shad, R. Butt, I. Ali, M.Z. Iqbal, Visible light photocatalytic degradation of crystal violet dye and electrochemical detection of ascorbic acid & glucose using BaWO4 nanorods, Mater. Res. Bull. 104 (2018) 38–43.
[41] V.R. de Mendonca, H.A. Mourao, A.R. Malagutti, C. Ribeiro, The role of the relative dye/photocatalyst concentration in TiO 2 assisted photodegradation process, Photochem. Photobiol. 90 (2014) 66–72.
[42] M.P. Yadav, N. Neghi, M. Kumar, G.K. Varghese, Photocatalytic-oxidation and photo-persulfate-oxidation of sulfadiazine in a laboratory-scale reactor: Analysis of catalyst support, oxidant dosage, removal-rate and degradation pathway, J. Environ. Manag. 222 (2018) 164–173.
[43] C. Chen, Y. Wang, Z. Yi, S. Wang, J. Ma, H. Gao, X. Wu, G. Liu, H. Yang, PH-induced structural evolution, photodegradation mechanism and application of bismuth molybdate photocatalyst, Adv. Powder Technol. 33 (2022) 103858.
[44] M. Goudarzi, H.A. Alshamsi, M. Amiri, M. Salavati-Niasari, ZnCo2O4/ZnO nanocomposite: Facile one-step green solid-state thermal decomposition synthesis using Dactylopius Coccus as capping agent, characterization and its 4T1 cells cytotoxicity investigation and anticancer activity, Arab. J. Chem. 14 (2021) 103316.
[45] H. Majdi, R. Salehi, M. Pourhassan-Moghaddam, S. Mahmoodi, Z. Poursalehi, S. Vasilescu, Antibody conjugated green synthesized chitosan-gold nanoparticles for optical biosensing, Colloid and Interface Science, Communications 33 (2019) 100207.
[46] N.D. Klein, K.R. Hurley, Z.V. Feng, C.L. Haynes, Dark field transmission electron microscopy as a tool for identifying inorganic nanoparticles in biological matrices, Anal. Chem. 87 (2015) 4356–4362.
[47] A. Samadi-Maybodi, A. Vahid, High yield synthesis and characterization of well-ordered Mesoporous silica nanoparticles using Sodium Carboxy Methyl Cellulose, J. Non-Cryst. Solids 357 (2011) 1827–1830.
[48] M. Khalfaoui, S. Knani, M. Hachicha, A.B. Lamine, New theoretical expressions for the five adsorption type isotherms classified by BET based on statistical physics treatment, J. Colloid Interface Sci. 263 (2003) 350–356.
[49] G. Chen, C. Dai, C. Ma, A stable half-metallic ferromagnetic material SrNiO3: a prediction from first principles. 2014 International Conference on Mechatronics, Electronic, Industrial and Control Engineering (MEIC-14), Atlantis Press, 2014, pp. 746–749.
[50] E. Cho, K. Klyukin, S. Ning, J. Li, R. Comin, R.J. Green, B. Yildiz, C.A. Ross, First-principles calculation of oxygen vacancy effects on the magnetic properties of the perovskite SrNiO 3, Physical Review, Materials 5 (2021) 094413.
[51] M.M. Rahman, M.M. Hussain, A.M. Asiri, A novel approach towards hydrazine sensor development using SrO·CNT nanocomposites, RSC Adv. 6 (2016) 65338–65348.
[52] A. Rahdar, M. Aliahmad, Y. Azizi, NiO nanoparticles: synthesis and characterization, 5 (2015) 145- 151.
[53] M. Jamdar, M. Goudarzi, E.A. Dawi, M.A. Mahdi, L.S. Jasim, M. Salavati-Niasari, Synthesis of SmMnO3/Sm2O3 nanocomposites as efficient photocatalysts for organic dye degradation by sol gel pechini method, Results Eng. 21 (2024) 101650.
[54] Y. Li, S. Yao, W. Wen, L. Xue, Y. Yan, Sol–gel combustion synthesis and visible-light-driven photocatalytic property of perovskite LaNiO3, J. Alloy. Compd. 491 (2010) 560–564.
[55] C. Chen, J. Zhou, J. Geng, R. Bao, Z. Wang, J. Xia, H. Li, Perovskite LaNiO3/TiO2 step-scheme heterojunction with enhanced photocatalytic activity, Appl. Surf. Sci. 503 (2020) 144287.
[56] M.C. Maridevaru, B. Aljafari, S. Anandan, M. Ashokkumar, Synergistic impacts of sonolysis aided photocatalytic degradation of water pollutant over perovskite-type CeNiO 3 nanospheres, N. J. Chem. 46 (2022) 10117–10127.
[57] D.J. Jovanovic, A. Chiappini, L. Zur, T.V. Gavrilović, L.T.N. Tran, A. Chiasera, A. Lukowiak, M.D. Dramićanin, M. Ferrari, Synthesis, structure and spectroscopic assessment of luminescent GdVO4: Dy3+ and DyVO4 nanoparticles, in: Fiber Lasers and Glass Photonics: Materials through Applications, SPIE, 2018, pp. 249–258.
[58] S. Kianipour, F.S. Razavi, I. Waleed, S.E. Izzat, I. Farhan, T.S. Hussein, K. Heydaryan, M. Salavati-Niasari, NdCoO3 nanostructures as promising candidate photocatalysts for boosting visible-light-driven photocatalytic degradation of organic pollutants, J. Sci.: Adv. Mater. Devices 7 (2022) 100506.
[59] Y. Li, S. Yao, W. Wen, L. Xue, Y. Yan, Sol–gel combustion synthesis and visible-light-driven photocatalytic property of perovskite LaNiO3, J. Alloy. Compd. 491 (2010) 560–564.
[60] B. Revathi, L. Balakrishnan, S. Pichaimuthu, A. Nirmala Grace, N. Krishna Chandar, Photocatalytic degradation of rhodamine B using BiMnO3 nanoparticles under UV and visible light irradiation, J. Mater. Sci.: Mater. Electron. 31 (2020) 22487–22497.
[61] Y. Yang, Y. Jiang, Y. Wang, Y. Sun, Photoinduced decomposition of BaFeO3 during photodegradation of methyl orange, J. Mol. Catal. A: Chem. 270 (2007) 56–60.
[62] C.R. Michel, M.A. Lopez-Alvarez, A.H. Martínez-Preciado, G.G. Carbajal-Arízaga, Novel UV Sensing and Photocatalytic Properties of DyCoO3, J. Sens. 2019 (2019) 5682645.
[63] J. Yang, X. Xie, P. Tang, H. Chen, C. Lv, Preparation of nanoparticulate DyMnO3 microwave-assisted method and its photocatalytic activity, Ferroelectrics 546 (2019) 231–238.
[64] M.C. Maridevaru, B. Aljafari, S. Anandan, M. Ashokkumar, Synergistic impacts of sonolysis aided photocatalytic degradation of water pollutant over perovskite-type CeNiO3 nanospheres, N. J. Chem. 46 (2022) 10117–10127.
[65] M.M. Hasan, A. Kabir, M. Kamruzzaman, The structural, elastic, electronic, magnetic and optical properties of $SrNiO_3$ perovskite: A DFT and DFT+U study, Results Phys. 41 (2022) 105920.